

Medical Image Fusion Method Based on Coupled Neural P Systems in Nonsubsampled Shearlet Transform Domain

Bo Li, Hong Peng*,†, Xiaohui Luo*, Jun Wang*,§, Xiaoxiao Song*,
Mario J. Pérez-Jiménez†,¶ and Agustín Riscos-Núñez†,||

*School of Computer and Software Engineering
Xihua University, Chengdu 610039, P. R. China

†Research Group of Natural Computing
Department of Computer Science and Artificial Intelligence
University of Seville, Sevilla 41012, Spain

‡ph.xhu@hotmail.com

§wj.xhu@hotmail.com

¶marper@us.es

||ariscosn@us.es

Accepted 1 June 2020

Published Online 18 August 2020

Coupled neural P (CNP) systems are a recently developed Turing-universal, distributed and parallel computing model, combining the spiking and coupled mechanisms of neurons. This paper focuses on how to apply CNP systems to handle the fusion of multi-modality medical images and proposes a novel image fusion method. Based on two CNP systems with local topology, an image fusion framework in nonsubsampled shearlet transform (NSST) domain is designed, where the two CNP systems are used to control the fusion of low-frequency NSST coefficients. The proposed fusion method is evaluated on 20 pairs of multi-modality medical images and compared with seven previous fusion methods and two deep-learning-based fusion methods. Quantitative and qualitative experimental results demonstrate the advantage of the proposed fusion method in terms of visual quality and fusion performance.

Keywords: Medical images; multi-modality; coupled neural P systems; nonsubsampled shearlet transform.

1. Introduction

With the rapid development of theories and applications in brain science, spiking neural networks (SNN)¹ have very solid theoretical and experimental basis and show more powerful computation and assistive memory ability than traditional artificial neural network.² Many recent advances have been made in modeling learning and computation with recurrently connected spiking neurons capable of performing a wide variety of tasks, such as learning algorithm,^{3–5}

EEG classification and detection,^{6,7} pattern representation⁸ and control systems.⁹

Spiking neural P (SNP) systems are a class of distributed parallel computing models inspired by spiking neurons.¹⁰ Except the topology of directed graph, each neuron in an SNP system has two components: data unit, storing the number of spikes, and spiking rules, of the form $E/a^c \rightarrow a^p$. The state of the system is characterized by data units and evolved by spiking rules. Therefore, SNP systems can be used as a modeling tool to characterize the

[‡]Corresponding author.

dynamic systems. In the past years, a variety of SNP systems have been proposed,^{11–13} for example, SNP systems with multiple channels,¹⁴ dynamic threshold neural P systems,¹⁵ SNP systems with rules on synapses,¹⁶ SNP systems with inhibitory rules¹⁷ and dendrite P systems.¹⁸ These variants have been theoretically proven to be Turing-universal number generating/accepting devices and function computing devices. Moreover, some variants have been used in several real-world problems, such as fault diagnosis,^{19–21} function optimization.²² This paper focusses on how to apply the variants of SNP systems to deal with the fusion of multi-modality medical images.

1.1. Related work

In the recent years, the fusion technology of multi-modality medical images has emerged as a hot research topic since the detection method based on multi-modality medical images has become a potential analysis tool against the critical diseases such as Cancer and Alzheimer, and so on. The fusion of multi-modality medical images aims to integrate complementary information from two or more medical images with different modalities to generate a fusion image. The fused image can provide more accurate information for physicians to clearly diagnose and treat diseases. Each imaging modality has own limitation and shows its specific information. Magnetic resonance image (MRI) exhibits internal body structures such as abdomen, liver, pancreas and other smooth tissues, while computed tomography (CT) highlights bony structures and other anatomical parts with high resolution. Positron emission tomography (PET) and single-photon emission computed tomography (SPECT) images provide functional information related to metabolism. However, they are often portrayed in pseudo color and typically have low-resolution.²³ These multi-modalities can provide complementary information. To provide higher diagnostic accuracy, many studies have tended to combine the analysis of images obtained from different modalities of the same patient, which led to the development of multi-modality medical image fusion.

To integrate two or more images with different modalities into a single fusion image, many fusion techniques have been proposed in the past years. Image fusion can be realized in three different levels:

pixel, feature and decision levels. Pixel-level methods directly combine information of the corresponding pixels in two or more images to a single image. Feature-level methods fuse source images according to the retrieved features such as edges, shapes, textures or regions. By contrast, decision-level methods fuse some representation based on decision rules. For each pixel-level fusion method, it is necessary to include the most important information in source images in a single image with the least change possible, especially distortion and loss. Thus, several pixel-level fusion methods have been proposed, such as multi-resolution singular value decomposition, guided filtering, sparse representation, and so forth.

Multi-scale transform (MST)-based fusion methods have been proposed with three stages: (i) source images are first decomposed into multi-scale representation with low-frequency and high-frequency information; (ii) multi-scale representations are then fused according to some fusion rules; (iii) inverse transform of the fused multi-scale coefficients is finally used to generate the fusion image. In the fusion methods, MST can extract useful image features from different scales and has good local characteristics. The MST includes Laplacian pyramid (LP),²⁴ gradient pyramid,²⁵ and wavelet transform.²⁶ The wavelet transform has become a popular fusion method, including the discrete wavelet transform (DWT)²⁷ and dual-tree complex wavelet transform.²⁸ However, these wavelet transforms have drawbacks in terms of nonshift-invariance, poor spatiality, and nontime-invariance. To overcome these drawbacks, several multi-scale transforms have been introduced in image fusion, including curvelet transform,²⁹ surfacelet transform,³⁰ nonsubsampled contourlet transform (NSCT),³¹ and sparse representations.³² Recently, nonsubsampled shearlet transform (NSST) has been developed to propose image fusion method because of its several excellent properties,³³ for example, shift invariance and the ability to capture higher dimensions of singularities (such as direction, edge, and detail information). This work aims to develop an image fusion method in NSST domain for multi-modality medical images.

In the recent years, several multi-modality medical image fusion methods have been developed. Singh and Khare³⁴ proposed a fusion method based on Daubechies complex wavelet transform (DCxWT)

for multi-modality medical images, which fused the complex wavelet coefficients of source images using maximum selection rule. Zhu *et al.*³⁵ proposed a dictionary learning-based image fusion method, where image patches were obtained by a sampling scheme and classified by a clustering algorithm, and then a dictionary was constructed by K-SVD. Manchanda *et al.*³⁶ discussed a fusion method of multi-modality medical images using fuzzy transform. Then, they presented an improved fusion algorithm for multi-modality medical images.³⁷ Li *et al.*³⁸ developed a medical image fusion, denoising, and enhancement method based on low-rank sparse component decomposition and dictionary learning. Singh and Anand³⁹ investigated a fusion method for multi-modality medical images, which utilized both the features extracted by the discrete ripplet transform (DRT) and pulse coupled neural network. Liu *et al.*⁴⁰ introduced a sparse representation model for pixel-level medical image fusion, named convolutional sparsity based morphological component analysis. Padmavathi *et al.*⁴¹ proposed an image fusion algorithm for constructing a fusion image through total variation (TV-L1) model using an optimized adaptive weighting scheme.

Recently, two deep-learning-based methods have been developed for image fusion. Li *et al.*⁴² presented a deep learning architecture for image fusion, including encoding network and decoding network, and the fusion method is called DenseFuse. Zhang *et al.*⁴³ presented a general image fusion framework based on convolutional neural networks (CNNs), called IFCNN. These deep-learning-based fusion methods have demonstrated a competitive fusion performance. However, they need very time-consuming training process compared with previous fusion methods.

1.2. Motivation

Coupled neural P (CNP) systems are a recently developed distributed parallel computing model,⁴⁴ combining the spiking and coupled mechanisms of neurons. Our previous work has proven that CNP systems are Turing-universal number generating/accepting devices and function computing devices. This paper focuses on application of CNP systems in the fusion task of multi-modality medical images, and proposes a novel CNP-system-based

fusion method in NSST domain for multi-modality medical images. For this goal, two CNP systems with local topology are designed to develop a fusion framework for multi-modality medical images. The fusion framework consists of three parts: (i) NSST transform; (ii) image fusion in NSST domain; (iii) inverse NSST transform. The low-frequency NSST coefficients of multi-modality medical images are regarded as the external inputs of two CNP systems and the corresponding outputs are used as control condition of fusion rules. The contribution of this paper can be summarized as follows:

- (i) CNP systems with local topology are designed, where low-frequency NSST coefficients of multi-modality medical images are their external inputs;
- (ii) A novel fusion framework in NSST domain for multi-modality medical images is developed, where two CNP systems are its key components.
- (iii) A fusion rule based on CNP system is developed, where the outputs of CNP systems are used to control the fusion rule.

The rest of this paper is organized as follows. Section 2 first introduces CNP systems with local topology, and then briefly reviews NSST transform. Section 3 describes in detail the proposed fusion framework in NSST domain for multi-modality medical images. Section 4 gives the experimental results. Conclusions and discussion are drawn in Sec. 5.

2. Methods

2.1. CNP systems with local topology

CNP systems as a variant of SNP systems,^{10,14} are a kind of Turing-universal, distributed parallel computing models.^{15–17} To deal with the fusion of multi-modality medical images, CNP systems are designed as an array of neurons with local topology, i.e. CNP systems with local topology.

Definition 1. An CNP system with local topology, of degree $m \times n$, is defined by

$$\Pi = (O, \sigma_{11}, \sigma_{12}, \dots, \sigma_{1n}, \dots, \sigma_{m1}, \dots, \sigma_{mn}, \text{syn}),$$

where

- (1) $O=\{a\}$ is an alphabet (the object a is known as the spike);

- (2) $\sigma_{11}, \sigma_{12}, \dots, \sigma_{mn}$ are an array of $m \times n$ coupled neurons of the form

$$\begin{aligned}\sigma_{ij} &= (u_{ij}, v_{ij}, \tau_{ij}, R_{ij}), \\ 1 \leq i \leq m, \quad 1 \leq j \leq n,\end{aligned}$$

where

- (a) $u_{ij} \in \mathbb{R}$ is the value of spikes in feeding input unit in neuron σ_{ij} ;
 - (b) $v_{ij} \in \mathbb{R}$ is the value of spikes in linking input unit in neuron σ_{ij} ;
 - (c) $\tau_{ij} \in \mathbb{R}$ is the value of spikes in dynamic threshold unit in neuron σ_{ij} ;
 - (d) R_{ij} denotes the finite set of spiking rules, of the form $E/(a^u, a^v, a^\tau) \rightarrow a^p$, where E is the firing condition, $p \geq 0$, $\tau \geq 0$, and $p \leq u(1+v)$.
- (3) $\text{syn} = \{(ij, kl) \mid 1 \leq i \leq m, 1 \leq j \leq n, |k-i| \leq r, |l-j| \leq r, i \neq k, j \neq l\}$, where r is the neighborhood radius. (synapses)

Suppose that I is a medical image with size $m \times n$, and $C = \{C_{ij}\}_{m \times n}$ is a matrix of low-frequency NSST coefficients of the image. Figure 1 shows the relationship between CNP system II and low-frequency NSST coefficient matrix C , where C has $m \times n$ low-frequency NSST coefficients, Π contains $m \times n$ coupled neurons, and neuron σ_{ij} is associated with low-frequency NSST coefficient C_{ij} , $1 \leq i \leq m$, $1 \leq j \leq n$.

In CNP system Π , each coupled neuron only communicates with its neighboring neurons, i.e. local topology. A r -neighborhood of neurons σ_{ij} is defined as follows, shown in Fig. 1:

$$\delta_r(\sigma_{ij}) = \{\sigma_{kl} \mid |k-i| \leq r, |l-j| \leq r\}. \quad (1)$$

Each coupled neuron σ_{ij} has three data units: feeding input unit u_{ij} , linking input unit v_{ij} , and

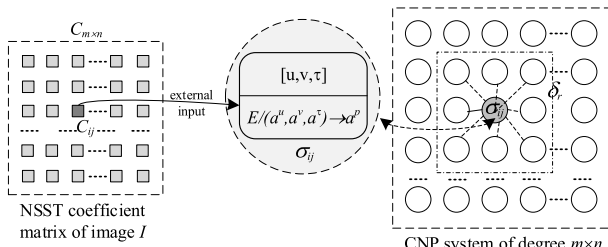


Fig. 1. An CNP system Π and the corresponding low-frequency NSST coefficient matrix C .

dynamic threshold unit τ_{ij} . Figure 1 presents the details of neuron σ_{ij} , including its three data units $[u_{ij}, v_{ij}, \tau_{ij}]$ and spiking rule $E/(a^u, a^v, a^\tau) \rightarrow a^p$. Neuron σ_{ij} has inputs of two types: (1) the spikes received from its neighboring neurons in δ_r and (2) an external stimulus, i.e. low-frequency NSST coefficient C_{ij} at position (i, j) , which is only related to its feeding input.

Neuron σ_{ij} has a spiking rule in the form of $E/(a^u, a^v, a^\tau) \rightarrow a^p$, where E is a firing condition denoted by $E \equiv (n_i(t) \geq \tau_i(t)) \wedge (u_i(t) \geq u) \wedge (v_i(t) \geq v) \wedge (\tau_i(t) \geq \tau)$, where $n_{ij}(t) = u_{ij}(t)(1 + v_{ij}(t))$, which represents a nonlinear modulation mechanism. If the firing condition is satisfied, then neuron σ_{ij} fires, meaning that spikes with the value u in the linking input unit, spikes with the value v in the linking input unit, spikes with the value τ in the dynamic threshold unit are consumed, and then spikes with the value p are produced and sent to its neighboring neurons. According to the spiking mechanism, the state equation for neuron σ_{ij} can be given by

$$\begin{aligned}u_{ij}(t+1) \\ = \begin{cases} u_{ij}(t) - u + C_{ij} \\ + \sum_{\sigma_{kl} \in \delta_r} w_{kl} p_{kl}(t), & \text{if } \sigma_{ij} \text{ fires,} \\ u_{ij}(t) + C_{ij} \\ + \sum_{\sigma_{kl} \in \delta_r} w_{kl} p_{kl}(t), & \text{otherwise,} \end{cases} \end{aligned} \quad (2)$$

$$\begin{aligned}v_{ij}(t+1) \\ = \begin{cases} v_{ij}(t) - v \\ + \sum_{\sigma_{kl} \in \delta_r} w_{kl} p_{kl}(t), & \text{if } \sigma_{ij} \text{ fires,} \\ v_{ij}(t) \\ + \sum_{\sigma_{kl} \in \delta_r} w_{kl} p_{kl}(t), & \text{otherwise,} \end{cases} \end{aligned} \quad (3)$$

$$\begin{aligned}\tau_{ij}(t+1) \\ = \begin{cases} \tau_{ij}(t) - \tau + p, & \text{if } \sigma_{ij} \text{ fires,} \\ \tau_{ij}(t), & \text{otherwise,} \end{cases} \end{aligned} \quad (4)$$

where $p_{kl}(t)$ is the value of the spikes received by neuron σ_{ij} from neighboring neuron σ_{kl} and $w_{kl}(t)$ is the corresponding local weight, and C_{ij} is an external

stimulus; p is the value of spikes generated by neuron σ_{ij} when it fires.

CNP system II has five *a priori* parameters: (i) iteration number t_{\max} , (ii) initial threshold τ_0 for each neuron, (iii) value of generated spikes p in spiking rule for each neuron, (iv) neighborhood radius r , and (v) local weight matrix $W_{r \times r}$.

The working procedure for CNP system II can be described as follows. Initially, for each neuron σ_{ij} , we set $u_{ij}(0) = v_{ij}(0) = 0$ and $\tau_{ij}(0) = \tau_0$, and assign $W_{r \times r}$. CNP system II starts from the initial state and operates iteratively until iteration number t_{\max} is reached. The system then halts. During the computation, the number of times that each neuron σ_{ij} fires is considered as its output and utilized as a control signal for the fusion of multi-modality medical images. For simplicity, a maximum consumption strategy is adopted in the application of spiking rules (i.e. set $u = u_{ij}(t)$, $v = v_{ij}(t)$, and $\tau = \tau_{ij}(t)$).

2.2. Nonsubsampled shearlet transform

Shearlet⁴⁵ is a relatively new multi-scale transform. Compared with some earlier multi-scale transforms for image representation such as pyramid, wavelet and curvelet, shearlet can capture the detailed information/features of an image at different directions more effectively and is capable of extracting a more optimal representation for the targeting image. The implementation process of shearlet transform (ST) is similar to that of contourlet transform, but the directional filters in contourlet are replaced by the shearing filters. An obvious advantage of shearlet over contourlet is that there are no restrictions on the number of directions in shearlet. Moreover, the inverse ST only needs a summation of the shearing filters, instead of inverting a directional filter bank in contourlet, which improves the computational efficiency.

Except from the above advantages, the subsampling method in the standard ST causes its lack of shift invariance. To overcome this defect, the nonsubsampled version of ST, known as NSST, has been introduced based on nonsubsampled pyramid filters (NSPFs) and shift-invariant shearlet filter banks (SFBs). Specifically, the NSPF is employed to generate the multi-scale decomposition of a source image from fine to coarse. If a l -level decomposition is applied, we can obtain $l+1$ subbands of the same size

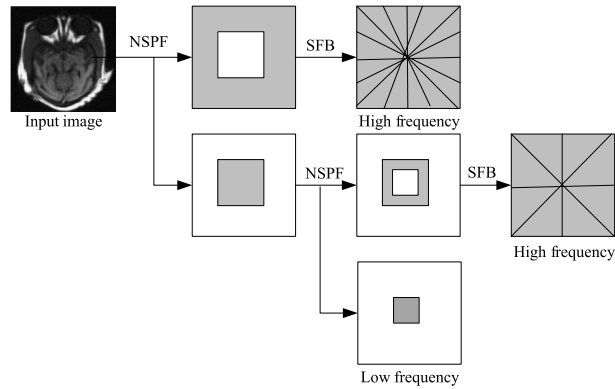


Fig. 2. Structure of two-level NSST decomposition.

as the source image, which includes l high-frequency subbands and one low-frequency subband. For each decomposition level, an SFB is applied to extract the multidirectional representations of the corresponding subband. Figure 2 shows the structure of a two-level NSST decomposition. The inverse NSST can precisely reconstruct the original image with two steps. The first step is to generate the nonsubsampled pyramid, where each scale is obtained by accumulating the filtered results of the decompositions at all directions using shearing filter banks. The second step is to reconstruct the image by the obtained nonsubsampled pyramid from coarse to fine using the reconstruction filters. More details about NSST could be found in Ref. 45.

3. The Proposed Fusion Method for Multi-Modality Medical Images

We propose an CNP-system-based image fusion framework in NSST domain for multi-modality medical images, shown in Fig. 3. The fusion framework includes three parts: (i) NSST transform; (ii) fusion rules; (iii) inverse NSST transform. In Fig. 3, source images are two multi-modality medical images, respectively.

Suppose that two source images, A and B , have the same size and have been registered. The multi-modality medical images are decomposed to the NSST coefficients by using NSST transform. Then, the NSST coefficients are fused to obtain the fused NSST coefficients. However, low-frequency NSST coefficients and high-frequency NSST coefficients are fused separately by different fusion rules. The low-frequency NSST coefficients are fused by an CNP system-based fusion rule, while the high-frequency

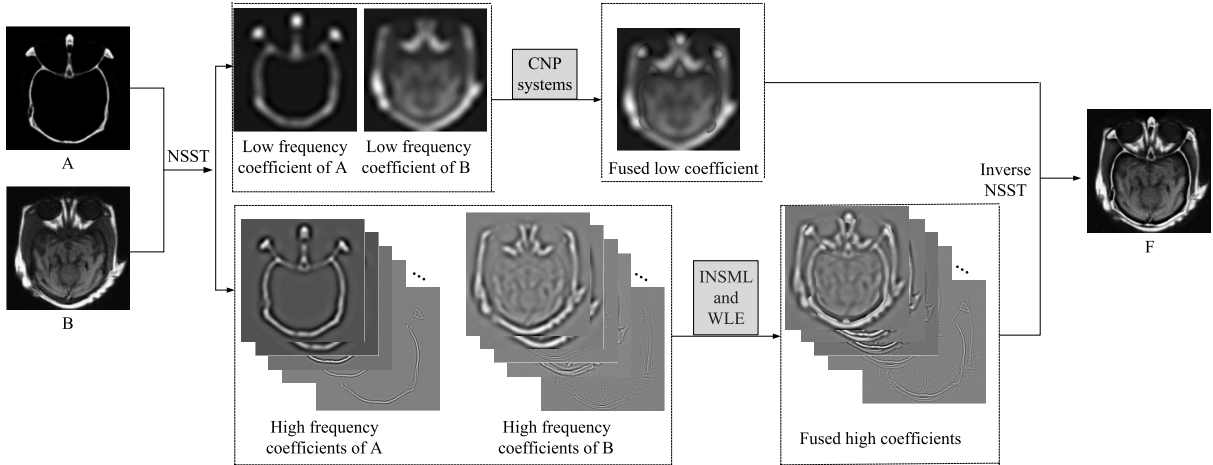


Fig. 3. The proposed fusion framework based on CNP systems in NSST domain for multi-modality medical images.

NSST coefficients adopt the WLE-INSML rules. CNP systems are a core component in the proposed fusion framework, and are used to control the fusion of low-frequency NSST coefficients. Two CNP systems, Π_1 and Π_2 , are considered to fuse low-frequency NSST coefficients of two multi-modality medical images, respectively. The fused NSST coefficients are converted back to reconstruct a fusion image by using inverse NSST transform.

Therefore, based on the fusion framework, the presented fusion method for multi-modality medical images has the following steps:

- NSST transform: two multi-modality medical images are decomposed to the NSST coefficients by using NSST transform, respectively; thus, we obtain low-frequency NSST coefficients and high-frequency NSST coefficients for each of multi-modality medical images.
- The fusion of low-frequency NSST coefficients: low-frequency NSST coefficients of two multi-modality medical images are regarded as external inputs of CNP systems Π_1 and Π_2 , respectively; the two CNP systems start from initial states, and then they are executed constantly until iteration number t_{\max} reaches; hence, they halt; outputs of the two CNP systems are used to control low-frequency fusion rules (see Eq. (5)).
- The fusion of high-frequency NSST coefficients: high-frequency NSST coefficients of two multi-modality medical images are fused by the WLE-INSML rules (see Eq. (9)).

- Inverse NSST transform: the fused coefficients are converted back to reconstruct a fusion image by using inverse NSST transform.

In the following, we describe in detail the used two fusion rules for low-frequency and high-frequency NSST coefficients.

3.1. Fusion rules for low-frequency NSST coefficients

Generally, fusion strategy for low-frequency NSST coefficients can have a big impact on final fusion images. In the proposed method, two key elements are considered, namely energy preservation and detail extraction. As we know, the energy is mainly contained in low-frequency NSST coefficients, and its intensity of different source images at the same position can be very different because source images are obtained by the different imaging mechanisms. The usual average-based fusion rules can cause a large loss of energy in the fused image. As a result, the brightness in some regions may drop sharply, leading to poor visual perception. To overcome the weakness, an CNP-system-based low-frequency fusion rule is developed in the proposed fusion framework.

Suppose that Π_A and Π_B are two CNP systems with local topology, which correspond to two multi-modality medical images, A and B , respectively. The low-frequency coefficients of two multi-modality medical images, respectively, are regarded as external inputs of Π_A and Π_B . Starting from initial state, the two CNP systems work constantly until iteration number t_{\max} reaches. Then, they halt. Denote

by T_A and T_B the excitation number matrixes associated with Π_A and Π_B , i.e. $T_A = (t_{ij}^A)_{m \times n}$ and $T_B = (t_{ij}^B)_{m \times n}$, where t_{ij}^A (respectively, t_{ij}^B) is the number of times that neuron σ_{ij} in Π_A (respectively, Π_B) fires. Based on the two excitation number matrixes, fusion rules for low-frequency NSST coefficients are defined as follows:

$$C_{l_0}^F(i, j) = \begin{cases} C_{l_0}^A(i, j), & \text{if } t_{ij}^A \geq t_{ij}^B, \\ C_{l_0}^B(i, j), & \text{if } t_{ij}^A < t_{ij}^B, \end{cases} \quad (5)$$

where $C_{l_0}^A(i, j)$ and $C_{l_0}^B(i, j)$ are low-frequency NSST coefficients of two multi-modality medical images at position (i, j) , respectively, and $C_{l_0}^F(i, j)$ are low-frequency NSST coefficients of the fused image F at position (i, j) , $1 \leq i \leq m$ and $1 \leq j \leq n$.

3.2. Fusion rules for high-frequency NSST coefficients

High-frequency coefficients contain the edges and contours of an image, which reflect the abundance of information at the corresponding location. To generate high-frequency fused images containing rich edges and textures, an activity-level measure, called WLE, is defined by

$$\text{WLE}_{lr}(i, j) = \sum_a \sum_b W'(a, b) C_{lr} \times (i + a, j + b)^2, \quad (6)$$

where $C_{lr}(i, j)$ is the high-frequency NSST coefficient in layer l and direction r at position (i, j) , and W' is a weight matrix and is defined as follows:

$$W' = \frac{1}{16} \begin{vmatrix} 1 & 2 & 1 \\ 2 & 4 & 2 \\ 1 & 2 & 1 \end{vmatrix}.$$

Due to some factors (e.g. computational efficiency), there always exists a limitation on the number of NSST decomposition level. Since high-frequency coefficients contain some detail information that cannot be extracted from the detailed image, an improved novel sum-modified Laplacian (INSML) is defined as follows:

$$\text{INSML}_{lr}(i, j) = \sum_a \sum_b W'(a, b) \text{IML}_{lr} \times (i + a, j + b), \quad (7)$$

where IML is given by

$$\begin{aligned} \text{IML}_{lr}(i, j) &= |2C_{lr}(i, j) - C_{lr}(i-1, j)| \\ &\quad - |C_{lr}(i+1, j)| + |2C_{lr}(i, j) - C_{lr}(i, j-1)| \\ &\quad + \frac{1}{\sqrt{2}} |2C_{lr}(i, j) - C_{lr}(i-1, j-1)| \\ &\quad - |C_{lr}(i+1, j+1)| + \frac{1}{\sqrt{2}} |2C_{lr}(i, j) - C_{lr}(i-1, j+1)| \\ &\quad - |C_{lr}(i+1, j-1)|, \end{aligned} \quad (8)$$

where $C_{lr}(i, j)$ is the high-frequency coefficient in layer l and direction r at position (i, j) . Note that diagonal coefficients and adjacent information are considered in $\text{IML}_{lr}(i, j)$ and a factor $\frac{1}{\sqrt{2}}$ is set for diagonal coefficients.

Suppose $\text{WLE-INSML}_{lr}^A(i, j) = \text{INSML}_{lr}^A(i, j) \cdot \text{WLE}_{lr}^A(i, j)$ and $\text{WLE-INSML}_{lr}^B(i, j) = \text{WLE}_{lr}^B(i, j) \cdot \text{INSML}_{lr}^B(i, j)$, which are associated with source images A and B . Based on the WLE and INSML values, fusion rules for high-frequency coefficients are defined as follows:

$$C_{lr}^F(i, j) = \begin{cases} C_{lr}^A(i, j), & \text{if } \text{WLE-INSML}_{lr}^A(i, j) \geq \text{WLE-INSML}_{lr}^B(i, j), \\ C_{lr}^B(i, j), & \text{otherwise,} \end{cases} \quad (9)$$

where $C_{lr}^A(i, j)$ and $C_{lr}^B(i, j)$ are high-frequency NSST coefficients of two multi-modality medical images in layer l , direction r at position (i, j) , respectively, and $C_{lr}^F(i, j)$ are the high-frequency coefficients of fusion image F in layer l , direction r and position (i, j) .

4. Experimental Results

To evaluate the effectiveness of the proposed fusion method, we used 20 pairs of multi-modality medical images in experiments, shown in Fig. 4, including CT and MRI images, MRI_T1 and MRI_T2 images, MRI and PET images, MRI and SPECT images. These images are with size 256×256 , downloaded from open source “<http://www.med.harvard.edu/aanlib/>”.

In experiments, we compared the proposed fusion method with nine the-state-of-the-art fusion

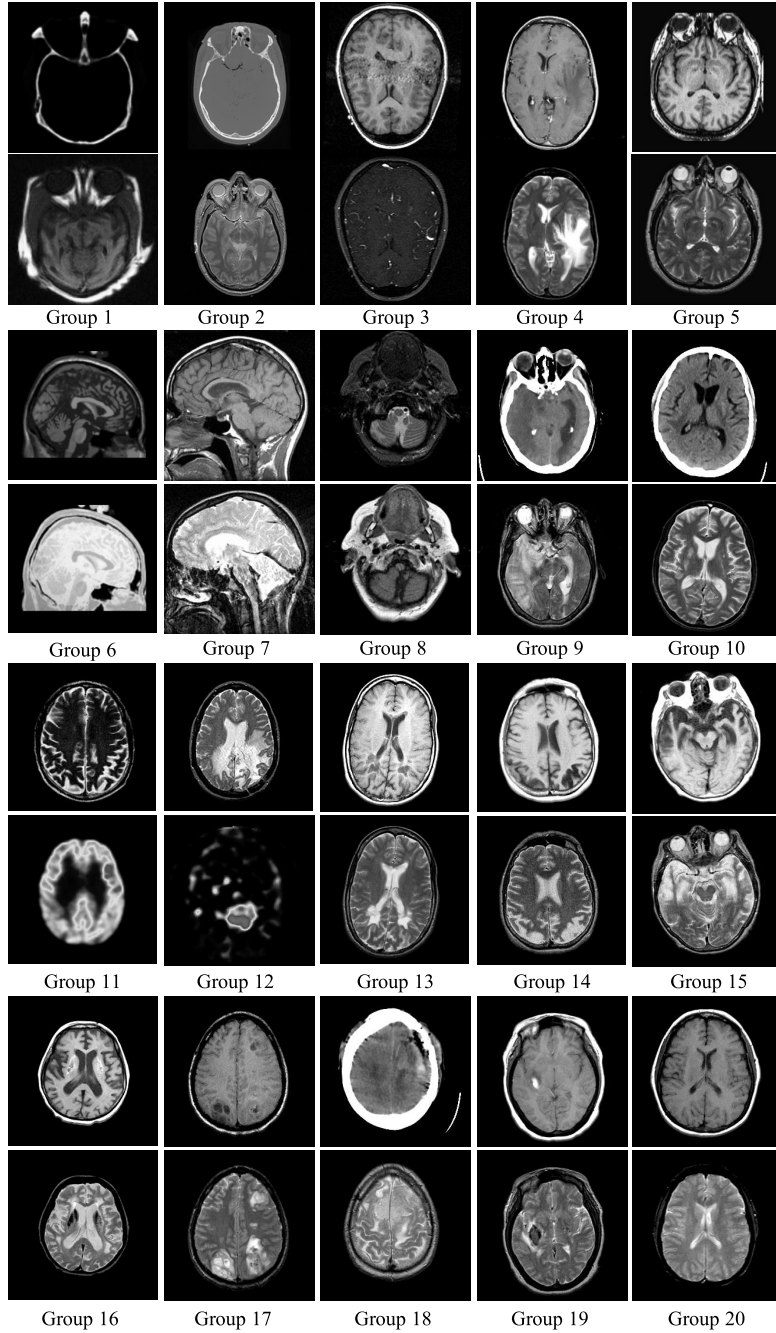


Fig. 4. Medical image dataset, consisting of 20 pairs of multi-modality medical images.

methods, including Wavelet,²⁶ DWT,⁴⁶ CVT,²⁹ DTCWT,²⁸ ASR,^{47,48} NSCT,³¹ NSST-PAPCNN⁴⁹ and deep-learning-based fusion methods (IFCNN⁴³ and DenseFuse⁴²).

The proposed fusion method is an CNP-system-based fusion method in NSST domain. It used the pyramid filter and directional filter of “maxflat” and

“[2 2 3 3]”, respectively. The parameters in CNP systems were set to $i_{\max} = 110$, $\tau_0 = 0.3$, $r = 7$ and $p = 1$. Moreover, $W_{7 \times 7} = \{w_{ij}\}_{7 \times 7}$ is determined as follows: (i) $w_{44} = 0$; (ii) $w_{ij} = 1/\sqrt{(i-4)^2 + (j-4)^2}$ for $i \neq 4, j \neq 4, 1 \leq i \leq 7, 1 \leq j \leq 7$.

The proposed fusion method was implemented in Matlab 2017b and on Inter Core i7-6700 CPU

3.4 GHz with 16 GB RAM. Except from two deep-learning-based fusion methods, other compared methods were also implemented on the same platform by using open source codes or the codes provided by authors. IFCNN and DenseFuse were implemented on Ubuntu 16.04 OS and on Inter Xeno Silver 4110 CPU 2.10 GHz and NVIDIA Tesla P100 with 16 GB RAM by the open source codes provided by authors.

In the experiments, five fusion quality metrics were used objectively to evaluate the proposed and compared fusion methods, including petrovics metric (Qabf),⁵⁰ feature mutual information (FMI),⁵¹ structural similarity index measure (MS_SSIM),⁵² spatial frequency⁵³ (SF) and standard deviation (SD).⁵⁴ For the five metrics, the larger the metric value, the better the fusion performance of the corresponding method.

In the first group of experiments, we compared the proposed method with seven previous fusion methods, including Wavelet, DWT, CVT, DTCWT, ASR, NSCT and NSST-PAPCNN. Four pairs of distinct types of medical images in data set were used, that is, “Group 1”, “Group 5”, “Group 11” and “Group 12”, which have the types of medical images, CT/MRI, MRI-T1/MRI-T2, MRI/PET and MRI/SPECT. The images fused by these methods are shown in Fig. 5–8. It can be observed from Fig. 5 that (1) some blurs exist in the image fused by DWT,

which leads to undesirable fusion result; (2) there is similar problem in fusion images (j), (k), (g), and (h): lower contrast and brightness. Note that the contrast means the distance between white and black points of the fusion image. In contrast, the image fused by the proposed method not only retains the detailed information of source images but also has a high contrast.

We can find in Fig. 6 that (1) for MRI-type medical image, the image fused by DWT has a certain extent of blurred results; (2) Wavelet and NSST-PAPCNN do not better preserve the details of source images; (3) the images fused by CVT, DTCWT, ASR, and NSCT have lower contrast and brightness. However, the proposed method can retain the detailed information of source images and have a high contrast.

From Fig. 7, it can be observed that (1) for MRI-type and PET-type medical images, some blurs exist in the image fused by DWT; (2) the image fused by Wavelet has lower contrast. In contrast, other methods achieve better fusion effect.

We can observe from Fig. 8 that for MRI-type and SPECT-type medical images, the images fused by other fusion images achieve basic fusion goal except from DWT. However, the images fused by Wavelet, CVT, DTCWT, ASR, and NSCT have lower contrast and brightness. In contrast, the proposed method visually achieves better fusion effect.

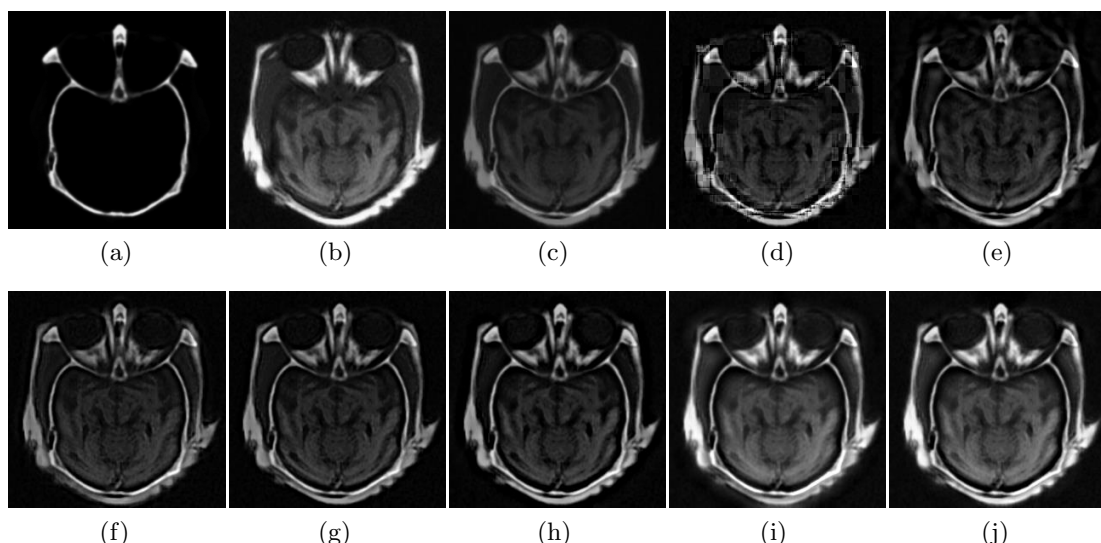


Fig. 5. The fusion results on “Group 1” images: (a) source CT image; (b) source MRI image; (c) Wavelet; (d) DWT; (e) CVT; (f) DTCWT; (g) ASR; (h) NSCT; (i) NSST-PAPCNN; (j) Proposed method.

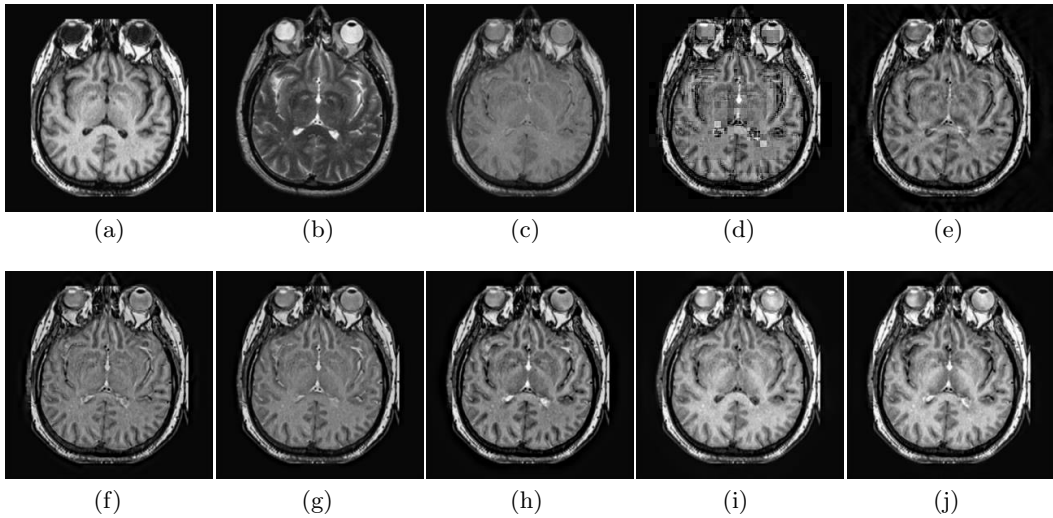


Fig. 6. The fusion results on “Group 5” images: (a) source MRI_T1 image; (b) source MRI_T2 image; (c) Wavelet; (d) DWT; (e) CVT; (f) DTCWT; (g) ASR; (h) NSCT; (i) NSST-PAPCNN; (j) Proposed method.

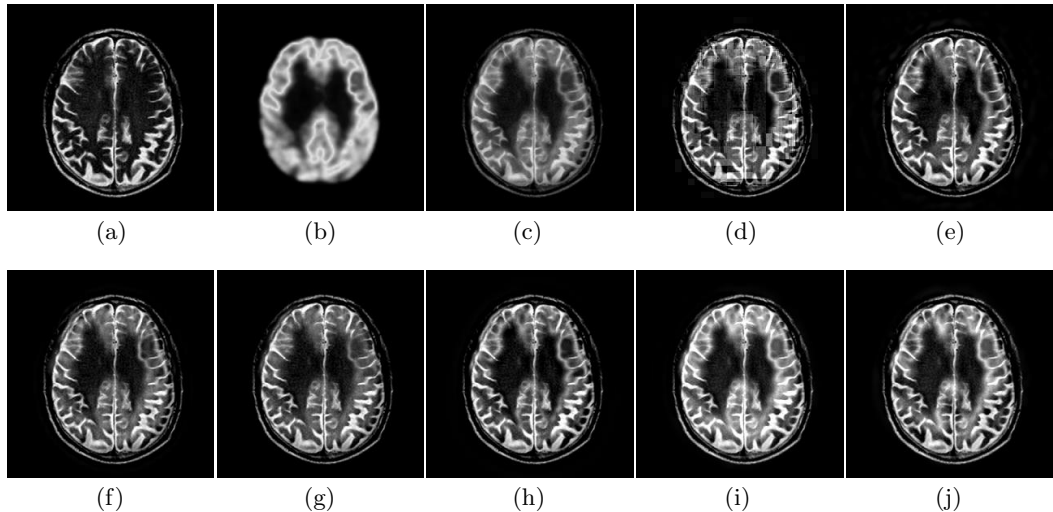


Fig. 7. The fusion results on “Group 11” images: (a) source MRI image; (b) source PET image; (c) Wavelet; (d) DWT; (e) CVT; (f) DTCWT; (g) ASR; (h) NSCT; (i) NSST-PAPCNN; (j) Proposed method.

It is difficult to judge the quality of the images fused by these methods from the subjective visual effect. Therefore, an objective assessment is necessary. Table 1 shows quantitative comparison of eight fusion methods for the four pairs of medical images in terms of five metrics. In Table 1, bold font marks that the corresponding method reaches the best metric value. It can be observed from Table 1 that

- (1) for “Group 1” (CT/MRI images), the proposed fusion method obtains the best value in terms of four metrics (Qabf, MS_SSIM, SF and SD).

- (2) for “Group 5” (MRI_T1/MRI_T2 images), the proposed fusion method obtains the best value in terms of three metrics (Qabf, MS_SSIM SF).
- (3) for “Group 11” (MRI/PET images), the proposed fusion method obtains the best value in terms of three metrics (Qabf, FMI and SF).
- (4) for “Group 12” (MRI/SPECT images), the proposed fusion method obtains the best value in terms of three metrics (MS_SSIM, SF and SD).

Recently, deep-learning-based image fusion methods have been developed and showed a good fusion

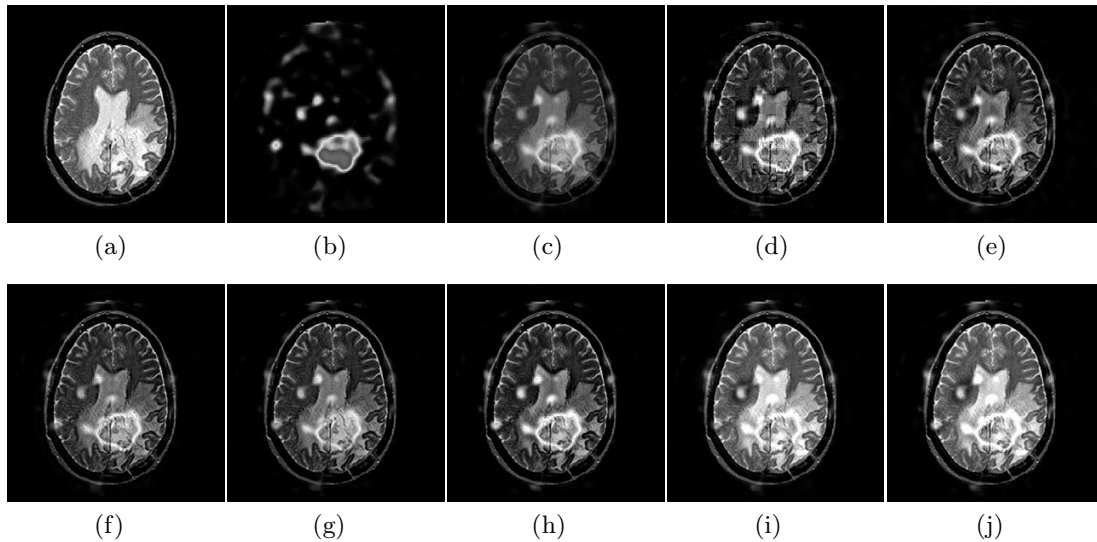


Fig. 8. The fusion results on “Group 12” images: (a) source MRI image; (b) source SPECT image; (c) Wavelet; (d) DWT; (e) CVT; (f) DTCWT; (g) ASR; (h) NSCT; (i) NSST-PAPCNN; (j) Proposed method.

Table 1. The comparison results of the proposed method with previous methods on four pairs of multi-modality medical images in terms of five metrics.

Images	Metrics	Wavelet	DWT	CVT	DTCWT	ASR	NSCT	NSST-PAPCNN	Proposed
Group 1 CT/MR1	Qabf	0.4038	0.5570	0.5593	0.6041	0.7068	0.7087	0.6873	0.7375
	FMI	0.9019	0.8766	0.8961	0.9038	0.9028	0.9050	0.9016	0.9038
	MS_SSIM	0.8638	0.8543	0.8445	0.8965	0.9355	0.9465	0.9249	0.9468
	SF	4.9565	6.7109	6.3395	6.0814	6.2640	6.4869	6.4558	6.7938
	SD	33.5205	45.4366	41.2239	37.7423	40.0486	45.0023	56.0239	57.6023
Group 5 MR1_T1/ MR2_T2	Qabf	0.3438	0.4717	0.4555	0.4823	0.5267	0.5289	0.5169	0.5326
	FMI	0.8457	0.8422	0.8529	0.8608	0.8653	0.8626	0.8554	0.8558
	MS_SSIM	0.8268	0.8264	0.8511	0.8681	0.8715	0.9191	0.9126	0.9229
	SF	6.5580	8.4866	8.3534	8.0793	7.6587	8.3378	8.3554	8.5287
	SD	53.5830	62.0562	59.8350	57.1968	57.2049	61.1839	73.5105	73.4071
Group 11 MR1/PET	Qabf	0.3825	0.5305	0.5844	0.5876	0.6231	0.6214	0.6104	0.6233
	FMI	0.8627	0.8421	0.8600	0.8617	0.8654	0.8627	0.8593	0.8659
	MS_SSIM	0.9196	0.8893	0.9015	0.9218	0.9085	0.9373	0.9400	0.9089
	SF	6.3380	7.6555	7.3994	7.3560	7.2614	7.4256	7.4974	7.7008
	SD	53.6637	61.2812	59.8996	58.1062	58.1046	61.0877	73.3523	66.3869
Group 12 MR1/SPECT	Qabf	0.4019	0.5939	0.6187	0.6464	0.6936	0.6902	0.7032	0.6911
	FMI	0.8708	0.8568	0.8690	0.8682	0.8718	0.8718	0.8847	0.8812
	MS_SSIM	0.9033	0.9267	0.9350	0.9426	0.9515	0.9628	0.9569	0.9631
	SF	5.6889	7.0786	7.0112	6.9655	6.8754	7.0389	7.0433	7.0907
	SD	43.9975	50.4934	48.7194	47.3968	47.6832	49.9952	69.4023	69.6387

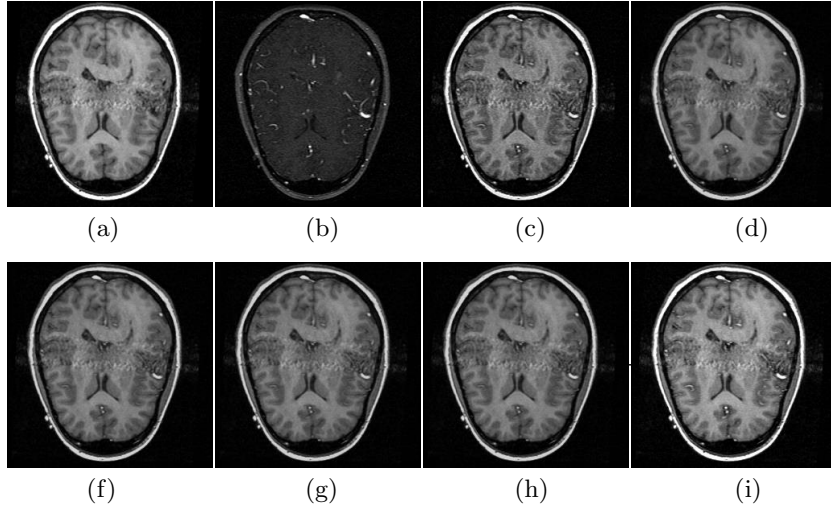


Fig. 9. The fusion results on “Group 3” images: (a) source CT image; (b) source MRI image; (c) IFCNN-Max; (d) DenseFuse- $1e0-l_1$ -norm; (e) DenseFuse- $1e1-l_1$ -norm; (f) DenseFuse- $1e2-l_1$ -norm; (g) DenseFuse- $1e3-l_1$ -norm; (h) Proposed method.

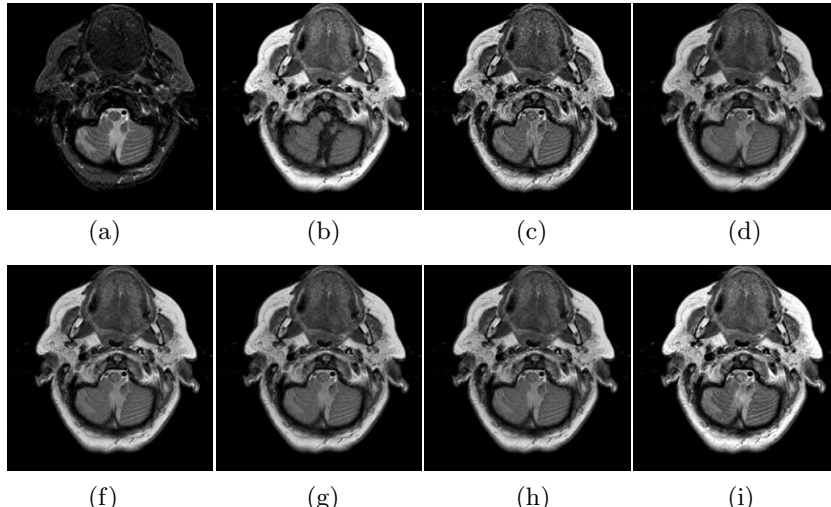


Fig. 10. The fusion results on “Group 8” images: (a) source MRI_T1 image; (b) source MRI_T2 image; (c) IFCNN-Max; (d) DenseFuse- $1e0-l_1$ -norm; (e) DenseFuse- $1e1-l_1$ -norm; (f) DenseFuse- $1e2-l_1$ -norm; (g) DenseFuse- $1e3-l_1$ -norm; (h) Proposed method.

effect. The proposed method was compared with two deep-learning-based methods, IFCNN⁴³ and DenseFuse.⁴² Four pairs of typical multi-modality medical images were used in the second group of experiments, “Group 3” (CT/MRI), “Group 8” (MRI_T1/MRI_T2) “Group 11” (MRI/PET) and “Group 12” (MRI/SPECT). Figures 9–12 show the images fused by the proposed method and two deep-learning-based methods on the four pairs of medical

images, where (a) and (b) are two source medical images with different multi-modalities.

From Figure 9, we can observe that the image fused by the proposed method has a higher contrast and retains more details compared with IFCNN and DenseFuse. For MRI_T1/MRI_T2 images in Fig. 10, it is difficult to identify the visual difference of the images fused by the three methods. For MRI/PET images in Fig. 11, DenseFuse has a relatively

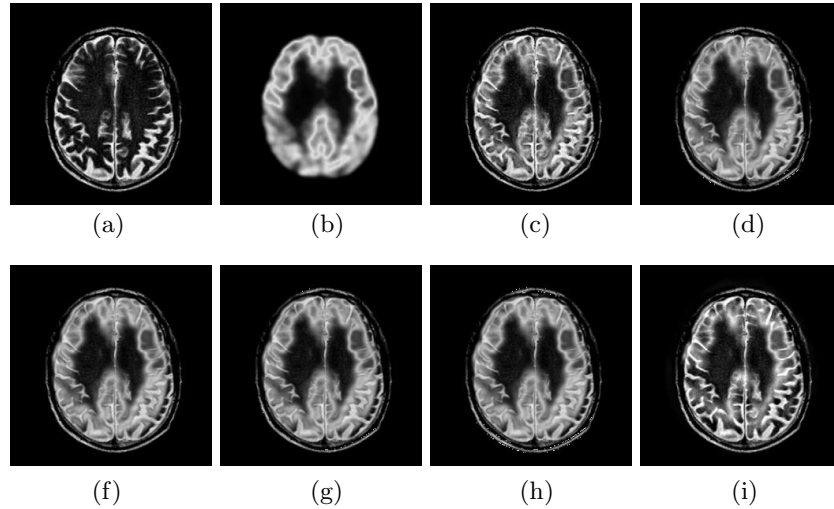


Fig. 11. The fusion results on “Group 11” images: (a) source MRI image; (b) source PET image; (c) IFCNN-Max; (d) DenseFuse- $1e0-l_1$ -norm; (e) DenseFuse- $1e1-l_1$ -norm; (f) DenseFuse- $1e2-l_1$ -norm; (g) DenseFuse- $1e3-l_1$ -norm; (h) Proposed method.

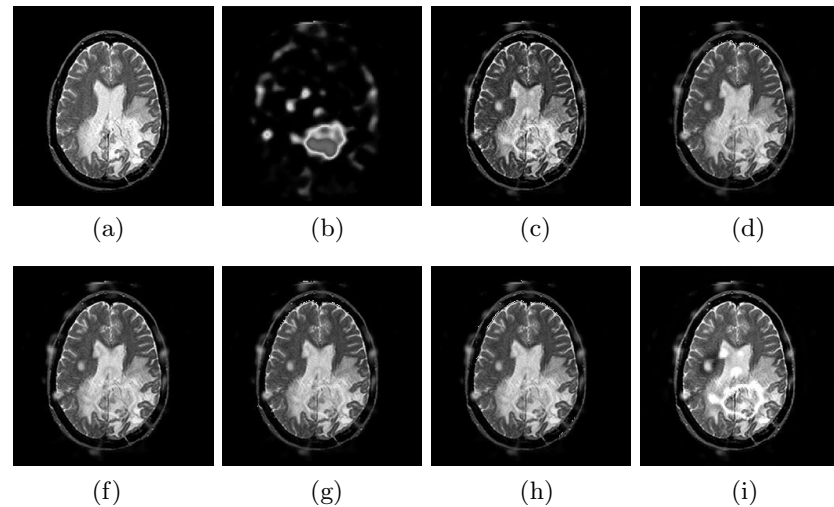


Fig. 12. The fusion results on “Group 12” images: (a) source MRI image; (b) source SPECT image; (c) IFCNN-Max; (d) DenseFuse- $1e0-l_1$ -norm; (e) DenseFuse- $1e1-l_1$ -norm; (f) DenseFuse- $1e2-l_1$ -norm; (g) DenseFuse- $1e3-l_1$ -norm; (h) Proposed method.

good fusion effect. In Fig. 12, the proposed method retains more details and has better contrast in comparison to IFCNN and DenseFuse. However, we cannot visually judge which method is the best or worst in the three fusion methods.

Table 2 provides quantitative comparison results of the proposed method with two deep-learning-based methods for four pairs of medical images in terms of five metrics. The bold font marks that the corresponding method reaches the best metric value. It can be found from Table 2 that

- (1) for “Group 3” (CT/MRI images), the proposed fusion method obtains the best value in terms of three metrics (FMI, MS_{SSIM} and SD).
- (2) for “Group 8” (MRI_T1/MRI_T2 images), the proposed fusion method obtains the best value in terms of three metrics (FMI, MS_{SSIM}, and SD).
- (3) for “Group 11” (MRI/PET images), the proposed fusion method obtains the best value in terms of three metrics (Qabf, FMI, and SD).

Table 2. The comparison results of the proposed approach with previous approaches on four pairs of multi-modality medical images in terms of five indices.

Images	Methods	Qabf	FMI	MS-SSIM	SF	SD
Group 3 CT/MR1	IFCNN-Max	0.5880	0.9020	0.9722	8.3088	61.5478
	$\lambda = 1e^0$	0.6238	0.9110	0.9652	6.9348	55.6247
	DenseFuse	0.6352	0.9112	0.9693	7.0245	56.7375
	l_1 -norm	0.6236	0.9105	0.9650	6.9326	55.5923
	$\lambda = 1e^3$	0.6318	0.9113	0.9690	7.0054	56.7538
Group 8 MR1_T1 /MR1_T2	Proposed	0.6168	0.9127	0.9793	8.1301	69.3218
	IFCNN-Max	0.5220	0.8370	0.9706	8.3634	63.5505
	$\lambda = 1e^0$	0.5812	0.8579	0.9626	7.3355	60.2687
	DenseFuse	0.5912	0.8584	0.9639	7.4402	61.7528
	l_1 -norm	0.5842	0.8588	0.9625	7.3509	0.4569
Group 11 MR1/PET	$\lambda = 1e^3$	0.5911	0.8582	0.9649	7.4276	61.9309
	Proposed	0.5686	0.8584	0.9779	8.1971	73.7425
	IFCNN-Max	0.5845	0.8513	0.9395	7.7010	65.0031
	$\lambda = 1e^0$	0.5147	0.8490	0.9108	6.8761	62.9332
	DenseFuse	0.5223	0.8507	0.9073	6.9639	64.2405
Group 12 MR1/SPECT	l_1 -norm	0.5140	0.8501	0.9123	6.8413	63.2758
	$\lambda = 1e^3$	0.4973	0.8440	0.8998	6.9029	64.7645
	Proposed	0.6233	0.8659	0.9089	7.7008	66.3869
	IFCNN-Max	0.6757	0.8603	0.9569	7.0790	59.2958
	$\lambda = 1e^0$	0.6751	0.8711	0.9288	6.6352	60.4715
Dataset	DenseFuse	0.6865	0.8737	0.9241	6.7759	63.1825
	l_1 -norm	0.6685	0.8692	0.9257	6.6382	60.9806
	$\lambda = 1e^3$	0.6637	0.8669	0.9233	6.6793	62.0675
	Proposed	0.6911	0.8812	0.9631	7.0907	69.6387

Table 3. The comparison results of mean fusion performances of the proposed method with previous methods on all 20 pairs of multi-modality medical images in terms of five metrics.

Images	Methods	Qabf	FMI	MS-SSIM	SF	SD
Dataset	Wavelet	0.4118	0.8744	0.8712	6.0562	58.0526
	DWT	0.5044	0.8663	0.8667	7.3985	65.5705
	CVT	0.5098	0.8742	0.8807	7.3526	63.1811
	DTCWT	0.5300	0.8785	0.8926	7.1858	61.1045
	ASR	0.5711	0.8813	0.8995	6.8023	61.4771
	NSCT	0.5672	0.8796	0.9341	7.3134	64.6565
	NSST-PAPCNN	0.5499	0.8780	0.9239	7.3291	78.1641
	IFCNN-Max	0.5572	0.8708	0.9276	7.4579	71.3558
	$\lambda = 1e^0$	0.5306	0.8783	0.8850	6.4075	67.7750
	DenseFuse	0.5427	0.8807	0.8839	6.4695	68.8420
Dataset	l_1 -norm	0.5322	0.8791	0.8855	6.3946	67.9439
	$\lambda = 1e^3$	0.5325	0.8775	0.8808	6.4370	68.9663
	Proposed	0.5712	0.8817	0.9163	7.4975	75.4472

Table 4. The comparison results of the proposed method with previous methods on all 20 pairs of multi-modality medical images in terms of mean execution time.

Methods	Wavelet	DWT	CVT	DTCWT	ASR	NSCT	NSST-PAPCNN	Proposed
Times/s	0.1929	0.3692	0.5127	0.0968	74.7628	1.3901	5.7198	6.4847

- (4) for “Group 12” (MRI/SPECT images), the proposed fusion method obtains the best value in terms of five metrics (Qabf, FMI, MS-SSIM, SF, and SD).

We also provide the comparison results of mean fusion performances of the proposed method with other methods (seven previous methods and two deep-learning-based methods) on all 20 pairs of medical images in terms of five metrics. It can be found from Table 3 that the proposed fusion method obtains the best value in terms of three metrics (Qabf, FMI, and SF) and gets the second best value in SD metric, and it has a relatively high value in MS-SSIM metric.

In summary, subjective and objective comparison results demonstrate that the proposed fusion method achieves a good fusion quality and performance for multi-modality medical images.

To evaluate the computational efficiency of the proposed fusion method, we provide a comparison of average execution time of it and seven previous fusion methods on dataset. However, two deep-learning-based methods (IFCNN and DenseFuse) are not included in this comparison because they require a very time-consuming training process. Table 4 indicates that the proposed method has a higher computational efficiency. Therefore, CNP systems can provide a competitive model for multi-modality medical images.

5. Conclusions and Discussion

CNP systems are a class of distributed parallel computing models. This paper investigated a novel fusion method based on CNP-systems in NSST domain for multi-modality medical images. Two CNP systems with local topology were designed as basic component of the proposed fusion framework for multi-modality medical images. In the fusion framework, the fusion rules of low-frequency NSST coefficients are controlled by the two CNP systems that

correspond to low-frequency NSST coefficients in two multi-modality medical images respectively.

In experiments, two groups of comparisons were designed: (1) the comparison to seven previous fusion methods; (2) the comparison to two deep-learning-based fusion methods; In the two groups of comparisons, subjective and quantitative evaluations were considered. The experimental results have demonstrated the advantages of the proposed fusion method for the fusion of multi-modality medical images. In terms of reasons, this is due to the following two aspects:

- (1) NSST transform can capture more details of the image and provide rich complementary information, which is beneficial for image fusion.
- (2) CNP systems are inspired from the spike firing mechanism of coupled neurons. For NSST coefficients, the rich complementary information can trigger more neurons in local region to fire. As a result, the corresponding region in the fused image will become clearer.

Therefore, the two aspects make the proposed fusion method show good fusion performance on multi-modality medical images.

Our further work will focus on how to extend the proposed idea to various multimedia applications. In the future, we will extend and apply our idea to other multimedia applications, such as image segmentation,⁵⁵ image dehaze,⁵⁶ and 3D nuclear image processing.⁵⁷

References

1. S. Ghosh-Dastidar and H. Adeli, Spiking Neural Networks, *Int. J. Neu. Syst.* **19**(4) (2009) 295–308.
2. Y. Todo, Z. Tang, H. Todo, J. Ji, K. Yamashita, Neurons with multiplicative interactions of nonlinear synapses, *Int. J. Neu. Syst.* **29**(8) (2019) 1950012, 1–18.
3. S. Ghosh-Dastidar and H. Adeli, A new supervised learning algorithm for multiple spiking neural networks with application in epilepsy and seizure detection, *Neu. Netw.* **22**(10) (2009) 1419–1431.

4. X. Zhang, G. Foderaro, C. Henriquez and S. Ferrari, A scalable weight-free learning algorithm for regulatory control of cell activity in spiking neuronal networks, *Int. J. Neu. Syst.* **28**(2) (2018) 1750015, 1–20.
5. M. Bernert and B. Yvert, An attention-based spiking neural network for unsupervised spike-sorting, *Int. J. Neu. Syst.* **29**(8) (2019) 1850059, 1–18.
6. S. Ghosh-Dastidar and H. Adeli, Improved spiking neural networks for EEG classification and epilepsy and seizure detection, *Integrat. Comput. Aided Eng.* **14**(3) (2007) 187–212.
7. H. Adeli and S. Ghosh-Dastidar, *Automated EEG-based Diagnosis of Neurological Disorders - Inventing the Future of Neurology* (CRC Press, Taylor & Francis, Boca Raton, Florida, 2010).
8. R. Hu, S. Chang, Q. Huang, H. Wang and J. He, Monitor-based spiking recurrent network for the representation of complex dynamic patterns, *Int. J. Neu. Syst.* **29**(8) (2019) 1950006, 1–22.
9. A. Geminiani, C. Casellato, A. Antonietti, E. D’Angelo and A. Pedrocchi, A multiple-plasticity spiking neural network embedded in a closed-loop control system to model cerebellar pathologies, *Int. J. Neu. Syst.* **28**(5) (2018) 1750017, 1–23.
10. M. Ionescu, Gh. Păun, T. Yokomori, Spiking neural P systems, *Fundamenta Inf.* **71** (2006) 279–308.
11. Gh. Păun, Spiking neural P systems with astrocyte-like control, *J. Univ. Comput. Sci.* **13**(11) (2007) 1707–1721.
12. L. Pan and Gh. Păun, Spiking neural P systems with anti-spikes, *Int. J. Comput. Commun. Control* **IV**(3) (2009) 273–282.
13. L. Pan, Gh. Păun, G. Zhang and F. Neri, Spiking neural p systems with communication on request, *Int. J. Neu. Syst.* **28**(8) (2017) 1750042, 1–13.
14. H. Peng, J. Yang, J. Wang, T. Wang, Z. Sun, X. Song, X. Luo and X. Huang, Spiking neural P systems with multiple channels, *Neu. Netw.* **95** (2017) 66–71.
15. H. Peng, J. Wang, M. J. Pérez-Jiménez and A. Riscos-Núñez, Dynamic threshold neural P systems, *Knowl. Based Syst.* **163** (2019) 875–884.
16. T. Song, L. Pan and Gh. Păun, Spiking neural P systems with rules on synapses, *Theor. Comput. Sci.* **529** (2014) 82–95.
17. H. Peng, B. Li, J. Wang, X. Song, T. Wang, L. Valencia-Cabrera, I. Pérez-Hurtado, A. Riscos-Núñez and M. J. Pérez-Jiménez, Spiking neural P systems with inhibitory rules, *Knowl. Based Syst.* **188** (2020) 105064, 1–17.
18. H. Peng, T. Bao, X. Luo, J. Wang, X. Song, A. Riscos-Núñez and M. J. Pérez-Jiménez, Dendrite P systems, *Neu. Netw.* **127** (2020) 110–120.
19. T. Wang, G. Zhang, J. Zhao, Z. He, J. Wang and M. J. Pérez-Jiménez, Fault diagnosis of electric power systems based on fuzzy reasoning spiking neural P systems, *IEEE Trans. Power Syst.* **30**(3) (2015) 1182–1194.
20. H. Peng, J. Wang, P. Shi, M. J. Pérez-Jiménez and A. Riscos-Núñez, Fault diagnosis of power systems using fuzzy tissue-like P systems, *Integrat. Comput. Aided Eng.* **24** (2017) 401–411.
21. H. Peng, J. Wang, J. Ming, P. Shi, M. J. Pérez-Jiménez, W. Yu and C. Tao, Fault diagnosis of power systems using intuitionistic fuzzy spiking neural P systems, *IEEE Trans. Smart Grid* **9**(5) (2018) 4777–4784.
22. G. Zhang, H. Rong, F. Neri and M. J. Pérez-Jiménez, An optimization spiking neural P system for approximately solving combinatorial optimization problems, *Int. J. Neu. Syst.* **24**(5) (2014) 1440006, 1–16.
23. A.P. James and B.V. Dasarathy, Medical image fusion: A survey of the state of the art, *Inf. Fusion* **19** (2014) 4–19.
24. A. Toe, Image fusion by a ratio of low-pass pyramid, *Pattern Recog. Lett.* **9** (1989) 245–253.
25. V. S. Petrovic and C. S. Xydeas, Gradient-based multiresolution image fusion, *IEEE Trans. Image Process.* **13**(2) (2004) 228–237.
26. P. Zeeuw, *Wavelets and Image Fusion* (CWI, Amsterdam (March), 1998).
27. R. Redondo, F. roubek, S. Fischer and G. Cristóbal, Multifocus image fusion using the log-gabor transform and a multisize windows technique, *Inf. Fusion* **10** (2009) 163–171.
28. J. J. Lewis, R. J. O’Callaghan, S. G. Nikolov, D. R. Bull and N. Canagarajah, Pixel- and region-based image fusion with complex wavelets, *Inf. Fusion* **8**(2) (2007) 119–130.
29. F. Nencini, A. Garzelli, S. Baronti and L. Alparone, Remote sensing image fusion using the curvelet transform, *Inf. Fusion* **8** (2007) 143–156.
30. B. Zhang, C. Zhang, Y. Liu, J. Wu and H. Liu, Multi-focus image fusion algorithm based on compound PCNN in surfacelet domain, *Optik* **125** (2014) 296–300.
31. Q. Zhang and B. Guo, Multifocus image fusion using the nonsubsampled contourlet transform, *Signal Process.* **89**(7) (2009) 1334–1346.
32. Q. Zhang, Y. Liu, R. S. Blum, J. Han and D. Tao, Sparse representation based multi-sensor image fusion for multi-focus and multi-modality images: A review, *Inf. Fusion* **40** (2018) 57–75.
33. X. Jin, G. Chen, J. Hou, Q. Jiang, D. Zhou and S. Yao, Multimodal sensor medical image fusion based on nonsubsampled shearlet transform and S-PCNNs in HSV space, *Signal Process.* **153** (2018) 379–395.
34. R. Singh and A. Khare, Fusion of multimodal medical images using Daubechies complex wavelet transform — a multiresolution approach, *Inf. Fusion* **19** (2014) 49–60.
35. Z. Zhu, Y. Chai, H. Yin, Y. Li and Z. Liu, A novel dictionary learning approach for multi-modality

- medical image fusion, *Neurocomputing* **214** (2016) 471–482.
- 36. M. Manchanda and R. Sharma, A novel method of multimodal medical image fusion using fuzzy transform, *J. Visual Commun. Image Represent.* **40** (2016) 197–217.
 - 37. M. Manchanda and R. Sharma, An improved multimodal medical image fusion algorithm based on fuzzy transform, *J. Visual Commun. Image Represent.* **51** (2018) 76–94.
 - 38. H. Li, X. He, D. Tao, Y. Tang and R. Wang, Joint medical image fusion, denoising and enhancement via discriminative low-rank sparse dictionaries learning, *Pattern Recogn.* **79** (2018) 130–146.
 - 39. S. Singh and R. S. Anand, Ripplet domain fusion approach for CT and MR medical image information, *Biomed. Signal Process. Control* **46** (2018) 281–292.
 - 40. Y. Liu, X. Chen, R. K. Ward, Z. Wang, Medical image fusion via convolutional sparsity based morphological component analysis, *IEEE Signal Process. Lett.* **26**(3) (2019) 485–489.
 - 41. K. Padmavathi, C.S. Asha, M.V. Karki, A novel medical image fusion by combining TV-L1 decomposed textures based on adaptive weighting scheme, *Eng. Sci. Technol.* **23**(1) (2019) 225–239.
 - 42. H. Li and X. Wu, Densefuse: A fusion approach to infrared and visible images, *IEEE Trans. Image Process.* **28**(5) (2019) 2614–2623.
 - 43. Y. Zhang and Y. Liu, IFCNN: A general image fusion framework based on convolutional neural network, *Inf. Fusion* **54** (2020) 99–118.
 - 44. H. Peng and J. Wang, Coupled neural P systems, *IEEE Trans. Neural Network. Learn. Syst.* **30**(6) (2019) 1672–1682.
 - 45. G. Easley, D. Labate and W.-Q. Lim, Sparse directional image representations using the discrete shearlet transform, *Appl. Comput. Harmonic Anal.* **25**(1) (2008) 25–46.
 - 46. X. Li, X. Tian, Y. Sun and Z. Tang, Medical image fusion by multi-resolution analysis of wavelets transform, in *Wavelet Analysis and Applications, Applied and Numerical Harmonic Analysis* (Birkhäuser, Basel, 2007), pp. 389–396.
 - 47. Y. Liu and Z. Wang, Simultaneous image fusion and denoising with adaptive sparse representation, *IET Image Process.* **9**(5) (2015) 347–357.
 - 48. Y. Liu, S. Liu and Z. Wang, A general framework for image fusion based on multi-scale transform and sparse representation, *Inf. Fusion* **24** (2015) 147–164.
 - 49. M. Yin, X. Liu, Y. Liu et al., Medical image fusion with parameter-adaptive pulse coupled neural network in nonsubsampled shearlet transform domain, *IEEE Trans. Instrument. Measure.* **68**(1) (2019) 49–64.
 - 50. C. Xydeas and V. Petrovic, Objective image fusion performance measure, *Electron. Lett.* **36**(4) (2009) 308–309.
 - 51. M. B. A. Haghigiat, A. Aghagolzadeh and H. Seyedarabi, A non-reference image fusion metric based on mutual information of image features, *Comput. Electric. Eng.* **37**(5) (2011) 744–756.
 - 52. K. Ma, K. Zeng and Z. Wang, Perceptual quality assessment for multi-exposure image fusion, *IEEE Trans. Image Process.* **24**(11) (2015) 3345–3356.
 - 53. T. Stathaki, *Image Fusion: Algorithms and Applications* (Academic Press, 2011).
 - 54. M. Deshmukh and U. Bhosale, Image fusion and image quality assessment of fused images, *Int. J. Signal Process. Image Process. Pattern Recog.* **4** (2010) 484–508.
 - 55. H. Yu, F. He and Y. Pan, A scalable region-based level set method using adaptive bilateral filter for noisy image segmentation, *Multimedia Tools Appl.* **79** (2020) 5743–5765.
 - 56. S. Zhang and F. He, DRCDN: Learning deep residual convolutional dehazing networks, *The Visual Computer*, 2019. Available at <https://doi.org/10.1007/s00371-019-01774-8>.
 - 57. O. M. Manzanera, S. K. Meles, K. L. Leenders, R. J. Renken, M. Pagani, D. Arnaldi and N. M. Maurits, Scaled subprofile modeling and convolutional neural networks for the identification of parkinson’s disease in 3d nuclear imaging data, *Int. J. Neu. Syst.* **29**(9) (2019) 1950010.